



Shear-driven vertical mixing and turbulent exchange over the continental slope in the northwestern Sea of Japan

Dmitry Stepanov¹ · Alexander Ostrovskii² · Evgeny Ryzhov¹ · Alexander Lazaryuk¹

Received: 27 January 2024 / Accepted: 2 September 2024 / Published online: 16 November 2024
© Springer-Verlag GmbH Germany, part of Springer Nature 2024

Abstract

Using fine-scale measurements in the northwestern Sea of Japan, we estimated the vertical mixing parameters in the sea water column extended from the lower part of the thermocline downward to the near-bottom layer above the continental slope. The vertical scales of the turbulent patches were determined together with the turbulent dissipation rate and diapycnal diffusivity based on the conductivity, temperature, and depth data obtained by an Aqualog moored profiler from April through October 2015. The Thorpe-scale method was used to estimate the vertical mixing parameters as well as the vertical heat and salt fluxes. The enhanced vertical mixing, as well as enhanced downward heat flux and upward salt flux, occurred below the mixed layer despite strong density stratification. By comparing the turbulent dissipation rate and diapycnal diffusivity estimates derived via the Thorpe-scale method and the estimates of the same parameters obtained earlier by applying the finescale parameterization method to the same dataset in addition to the collocates of the current velocity measurements, the comparative accuracy evaluation of both methods was carried out. Finally, by compiling the vertical mixing data obtained by the Thorpe-scale method and the finescale parameterization approach, the generalized depth profile for the diapycnal diffusivity is presented for the depth range from 70 to 350 m.

Keywords Vertical mixing · The Sea of Japan · Thorpe-scale method · Finescale parameterization

1 Introduction

Located at the northwestern margin of the Pacific, the deep semi-enclosed Sea of Japan (hereinafter referred to as the

Responsible Editor: Zhiyu Liu

Alexander Ostrovskii, Evgeny Ryzhov and Alexander Lazaryuk contributed equally to this work

✉ Dmitry Stepanov
step-nov@poi.dvo.ru
Alexander Ostrovskii
osasha@ocean.ru
Evgeny Ryzhov
ryzhovea@poi.dvo.ru
Alexander Lazaryuk
lazaryuk@poi.dvo.ru

¹ V.I.Ilichev Pacific Oceanological Institute, Far Eastern Branch, Russian Academy of Sciences, 43, Baltiyskaya Street, Vladivostok 690041, Russia

² Shirshov Institute of Oceanology, Russian Academy of Sciences, 36 Nahimovskiy Prospekt, Moscow 117997, Russia

Sea) is renowned to the world oceanographers as a basin that provides opportunities for researchers to conduct large-scale oceanographic experiments (Gamo et al. 2014). The Sea dynamics feature processes typical of the ocean (Chang et al. 2015). Among these, one of the most interesting is the strong ventilation of the Sea intermediate and deep layers. The ventilation was thought to be associated with a circulation system, which keeps the deep water homogeneous (Takematsu et al. 1999). In the winter, during intensive northeasterly monsoon cooling, deep convection develops in the northwestern part of the Sea. Cold and fresh water as well as chemical tracers penetrate more than 1000 m below the surface (Talley et al. 2003, 2006). It is believed that deep convection began to slow in the 1960s or earlier (Kim et al. 2001, 2002), yet the intermediate and deep layers of the Sea remain well mixed. This implies that turbulent mixing could have become relatively more important in the past several decades in the Sea.

In the deep ocean, vertical mixing is generally caused by wind forcing and breaking of internal gravity waves, which are generated by the tide-topography interactions (Wunsch and Ferrari 2004; Waterhouse et al. 2014; MacKinnon et al. 2017; Gregg et al. 2018). In particular, internal lee waves

can be driven by the interaction of shear currents with the topography (Nikurashin et al. 2014; MacKinnon et al. 2017). Notably, the semidiurnal tide enters the Sea through the wide Tsushima Strait in the southern region and then propagates toward the northern continental slope. Although the tide wave weakens when it passes northward through the Sea, its energy is still high when it arrives at the continental slope and shelf (Jeon et al. 2014), where it induces internal gravity waves. Ostrovskii et al. (2021) assessed the turbulent mixing that can be generated by the shear-driven instabilities associated with breaking internal gravity waves over the Sea continental slope. The finescale parametrization framework (FSP) (Heney et al. 1986; Polzin et al. 1995; Kunze et al. 2002; Hibiya et al. 2012; MacKinnon et al. 2013; Polzin et al. 2014; Meyer et al. 2015; Gregg et al. 2018) that assumes that internal gravity wave breaking makes a major contribution to vertical mixing was applied to the *in situ* data for the thermal structure and the current shear to assess the turbulent dissipation rate and diapycnal diffusivity.

The estimates of diapycnal diffusivity indicated that the vertical exchange of heat, salt and dissolved oxygen was enhanced under the seasonal pycnocline in the warm half-year. Mesoscale eddies can also affect vertical mixing (Kunze et al. 1995; Whalen et al. 2015; Yang et al. 2017; You et al. 2021). Anticyclonic mesoscale eddies are well-developed in the northern Japan basin, and the data show that turbulent mixing is stronger at the edges and bottom parts of eddies (Ostrovskii et al. 2021, 2023).

In addition to the above-mentioned processes, vertical mixing can be driven by double diffusion (Inoue et al. 2007; Radko and Smith 2012; Lee et al. 2014). Double diffusion signatures were also found in the Sea (Stepanov et al. 2023). Using the above-mentioned Aqualog profiler dataset, Stepanov et al. (2023) studied fine-scale mixing associated with double diffusion processes: salt fingers and thermal convection. Based on the Turner angle analysis and estimates of the effective diffusivities of heat and salt (Inoue et al. 2007) derived from moored profiler Aqualog data, it was found that in the spring, thermal convection dominated the vertical mixing in the upper layer of the Sea between 70 m and 200 m. Double diffusion processes occurred sporadically in the upper layer, while shear-driven instabilities played the leading role in vertical mixing generation.

In this study, we focused on the estimation of the vertical mixing and turbulent exchange in the upper part of the Sea immediately below the near-surface layer through a further analysis of the moored profiler Aqualog dataset. The upper part of the Sea water column was not considered in the previous study (Ostrovskii et al. 2021) due to the limitations of the FSP framework. In the following, we apply the Thorpe-scale method (TSM) (Thorpe 1977; Thompson et al. 2007; MacKinnon et al. 2017; Smith 2020) to the depth profiles of the water density to estimate the turbulent patch

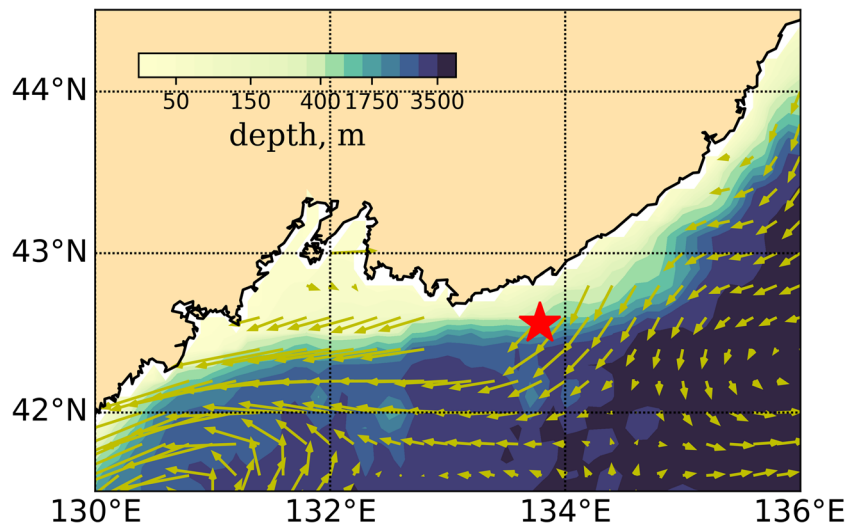
vertical scale by applying a special reordering of the data, as described below. The derived estimates are used to assess the turbulent dissipation rate. This approach requires high-resolution depth profiles of temperature and salinity with the background of a large vertical density gradient (Dillon 1982; Stansfield et al. 2001; Thompson et al. 2007). The TSM allows us to quantify the manifestations of turbulence regardless of its cause, assuming that these manifestations are associated with density overturns in the turbulent area. For clarity, to focus on turbulent mixing only, the time periods in which thermal convection and salt fingers prevailed in vertical mixing (Stepanov et al. 2023) must be excluded from this analysis. The estimates of the vertical mixing parameters derived using the TSM are compared with those obtained within the FSP framework. Therefore, we aim to obtain a more comprehensive overview of the vertical mixing in the intermediate waters in the northwestern Sea during the warm half-year.

The rest of the paper is organized as follows. The dataset used is presented in Sect. 2. The Thorpe-scale method and the FSP framework are described in Sect. 3. The conditions for the shear-driven turbulence, estimates of the turbulent dissipation rate and diapycnal diffusivity as well as the vertical heat and salt fluxes and their depth and temporal variations during the survey are presented in Sect. 4. The discussion in Sect. 5 is based on a comparison of the vertical mixing estimates derived from the TSM and the FSP framework. Additionally, the vertical distribution of the mixing processes is presented. Sect. 6 summarizes our findings.

2 Dataset

To quantify vertical mixing, we analyzed data of fine-structure measurements of temperature (T_m) and salinity (S) collected by an Aqualog profiler during a survey from mid-April to mid-October 2015. The Aqualog profiler was moored on the continental slope in the northwestern Sea (Fig. 1). The depth of the mooring station was approximately 425 m. The profiler crawled up and down a taut mooring wire at a vertical speed of about 0.2 m s^{-1} . During the first five days, the Aqualog profiler moved from 70 to 260 m, and on the sixth day, the profiler moved further downward to 420 m to obtain full-depth data profiles. This regular operation schedule was repeated until mid-October. In total, 1550 sets of vertical profiles of the measured parameters were obtained. The profiler was equipped with a Sea-Bird Electronics (SBE) CTD 52-MP, maintaining a sampling rate of 1 Hz, and a Nortek Aquadop, with the acoustic sampling rate of 23 Hz and the internal compass and inclinometer sampling rate of 4 Hz. Given the average vertical speed of about 0.2 m s^{-1} , the vertical resolution cast is about 20 cm. A detailed descrip-

Fig. 1 Survey-averaged geostrophic circulation data were obtained from the AVISO dataset (<https://www.aviso.altimetry.fr/en/data/data-access.html>), and the colored topography was obtained from the ETOPO1 (Amante and Eakins 2009) in the northwestern Sea. The location of the Aqualog profiler mooring station is shown by the red asterisk



tion of the survey measurements can be found in Ostrovskii et al. (2021). The SBE CTD 52-MP is a conductivity (C_m), T_m , pressure (P_m) sensor suit (SeaBird 2010). The salinity spiking (set of temperature and salinity pairs that has the same density e.g., warmer and saltier water versus fresher and colder water) arises from any mismatch in the sensor responses. In order to minimize salinity spiking, the CTD probe incorporates pump-controlled TC-ducted flow. T_m and C_m measurement resolutions are equal to $0.0001\text{ }^\circ\text{C}$ and 0.00005 S m^{-1} , respectively. According to SeaBird (2010), the accuracies of the measurements are $0.002\text{ }^\circ\text{C}$ and 0.0003 S m^{-1} , respectively. During the survey T_m and C_m varied from 0.7 to $5.5\text{ }^\circ\text{C}$ and from 2.91 to 3.25 S m^{-1} , respectively. The CTD probe maintains a low level of noise for the measured variables as follows: $0.0005\text{ }^\circ\text{C}$ and 0.0001 S m^{-1} . Because the SBE’s data processing software is not applicable to the data from the SB CTD 52-MP (SeaBird 2010), special software was developed to process the raw data.

In order to minimize errors owing to the response time and cell thermal mass effects the exponential filtering was applied

$$C_s(t) = C_s(t - \delta t) \cdot \exp(-\delta t/R_s) + C_m(t) \cdot (1 - \exp(-\delta t/R_s)), \quad (1)$$

where δt is the sampling interval and R_s varied from 0.2 to 0.5 was chosen to reduce salinity noise. In order to minimize error from the cell thermal mass effect, the data processing was applied as follows

$$C_{sc}(t) = C_s(t) + 10 \cdot A_c(t), \quad (2)$$

where

$$A_c(t) = \frac{0.2a}{b+2} (T_m(t) - T_m(t - \delta t)) (1 + 0.006 \cdot (T_m(t) - 20.0)) - \frac{b-2}{b+2} A_c(t - \delta t), \quad (3)$$

with coefficients: $a = 0.1$ and $b = 1/13$. Practical salinity was calculated from C_{sc} using UNESCO algorithms (Fofonoff and Millard Jr. 1983). All of the data profiles including the full-depth profiles were used to quantify vertical mixing. The potential density (σ_θ) was calculated from the T_m and S data using the Thermodynamic Equation of Sea-Water 2010 (TEOS-10) (McDougall and Barker 2011). The data processing allowed us to reduce the dynamical error (Yaroshchuk et al. 2023) of the potential density down to 10^{-3} kg m^{-3} .

3 Thorpe-scale method and the finescale parameterization framework

The depth profiles of the potential density were used to estimate the Thorpe scale (L_T), the turbulent dissipation rate (ε_K) and the diapycnal diffusivity (K_ρ). The diapycnal diffusivity is related to the turbulent dissipation rate via the parametrization by Osborn (1980) as follows:

$$K_\rho = \Gamma \varepsilon_K / N^2, \quad (4)$$

where Γ is the mixing efficiency and N is the buoyancy frequency. Γ is typically equal to 0.2 . Note that N represents the background stratification. In order to adjust vertical mixing estimations derived from the FSP framework and the Thorpe scale method, the background stratification N was estimated using the vertical scale of 36 dbar following (Ostrovskii et al. 2021). Then a 14-day window is used for the time averaging of N^2 . This time window exceeds the typical time scale of the eddy propagation over the moored station in the study area (Trusenkova et al. 2021; Ostrovskii et al. 2023).

We assess ε_K according to the method of Dougherty (1961) and Ozmidov (1965), assuming that there is a ver-

tical scale (L_O) for which stratification inhibits the extent of the turbulent patch:

$$L_O = \left(\varepsilon_K / N^3 \right)^{1/2}. \quad (5)$$

Thorpe (1977) suggested that scale (5) can be estimated by reordering a depth profile of density σ_θ , which contains a turbulent patch, to the steady density profile as follows:

$$L_T = \langle (z_n - z_m)^2 \rangle_z^{1/2}, \quad n \in R \quad (6)$$

where $\langle \dots \rangle_z$ denotes the average over the turbulent patch and R is the set of the fluid elements within the turbulent patch. These fluid elements are located at depths z_n and after reordering the density profile, the fluid elements are located at depths z_m (for example, Fig. 2). Based on direct dissipation measurements in a sheared thermocline, Dillon (1982) proposed the relation between the L_T and L_O , namely $L_O \approx 0.8L_T$. Using relation (5), ε_K can be estimated as follows:

$$\varepsilon_K = L_O^2 N^3 \approx 0.64 L_T^2 N^3. \quad (7)$$

Note that in Eqs. 5 and 7, N is the stratification of the specific turbulent patch (Thompson et al. 2007). To estimate N the concept of an equivalent linear stratification (Mater et al. 2015) is used. Smith (2020) modified this concept with reordered density profiles and least squares fits of lines (his Eq. (20)).

In applying the TSM, one may encounter the cases of "salinity spiking" in the raw data depth profiles when different ensembles of the T and S data may have the same density. To avoid an undesirable effect, the median filtering using 7-point median was applied to the salinity profiles; the

procedure efficient for eliminating spikes and reducing noise (Smith 2020). Also, the first 30 and last 180 data samples were excluded from each profile of T and S . The minimal valid length of the estimated turbulent patch is more than 0.8 m. It takes into account that the minimal value of the estimated rate of the turbulent dissipation is of the order of 10^{-12} W kg^{-1} . Finally, while using the TSM we have to consider the cases when the turbulence is maintained by a shear-driven mechanism and exclude other processes from consideration as will be described below.

Thorpe (1977) noted that his method cannot be applied in the regions dominated by thermal convection and double diffusion. Based on these results (Stepanov et al. 2023), events associated with double diffusion processes, i.e., diffusion convection and salt fingers, were omitted from further consideration. We also exclude the turbulent patches where the necessary condition for double diffusion is satisfied. The Turner angle (Ruddick 1983; Stepanov et al. 2023) was estimated using the TEOS-10 algorithm (McDougall and Barker 2011).

All of the profiles (ε_K or K_ρ) are binned into 10-m layers. The confidence intervals (95% level) of the median values are estimated using the bootstrap technique (Efron and Gong 1983) and the bootstrap toolbox (Zoubir and Boashash 1998).

When diapycnal diffusivity (4) is known, the vertical heat and salt fluxes can be estimated as follows:

$$Q = -c_p \rho_0 K_\rho \left\langle \frac{\partial \theta}{\partial z} \right\rangle_t, \quad J_S = -K_\rho \left\langle \frac{\partial S}{\partial z} \right\rangle_t, \quad (8)$$

where $\langle \dots \rangle_t$ denotes the time average, θ is the potential temperature, c_p is the specific heat of seawater which is equal to $4000 \text{ J kg}^{-1} \text{ K}^{-1}$ and ρ_0 is the seawater density of 1025 kg m^{-3} . Note that the θ and S data are binned into 2-dbar layers. The vertical gradients of θ and S are calculated over a

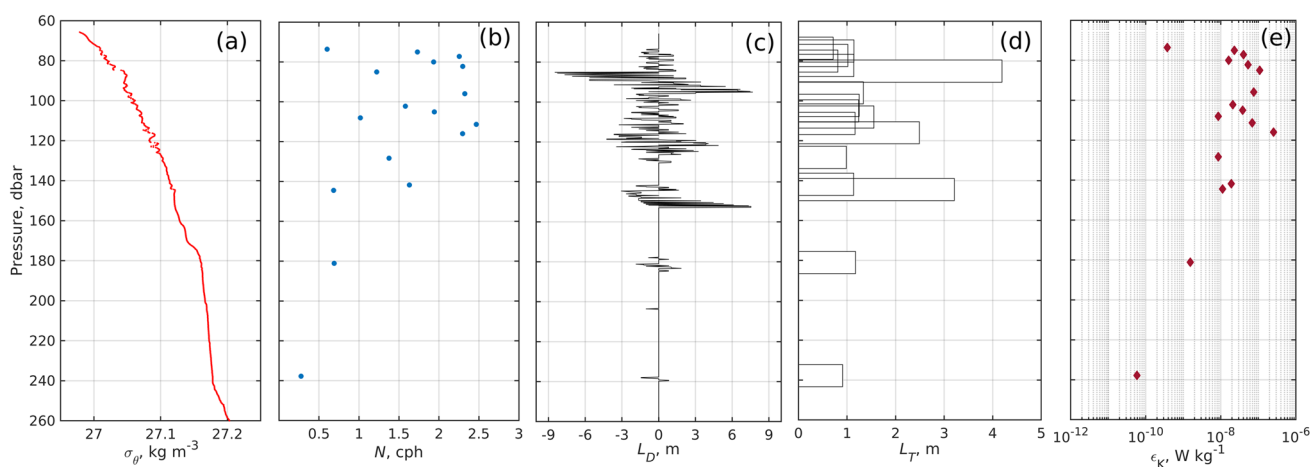


Fig. 2 An example of a density profile (σ_θ) (a) at 00 h 18 s on 26 April 2015 and the buoyancy frequency (N) (b) of the turbulent patches, Thorpe displacement ($L_D = (z_n - z_m)$) (c), Thorpe scale (L_T) (d), and

dissipation rate (ε_K) (e) obtained using Thorpe scale analysis. The turbulent patches with $N < 10^{-1}$ cph and $L_D, L_T < 0.7$ m were excluded from the analysis

10-dbar scale and a 14-day window is used for the time averaging of the vertical gradients. L_T , ε_K and K_ρ are estimated for each profile of σ_θ .

For a more detailed explanation of the TSM framework, let us consider an example of σ_θ and the profiles derived by applying the Thorpe scale analysis. The profile of σ_θ (Fig. 2) was obtained during an Aqualog profiler descent around midnight on April 26, 2015. This profile reveals features of shear-driven turbulence within the depth range from 70 to 160 m. For example, from 80 to 100 m, the value of σ_θ at the specified depth level is greater than that at the next depth level. The density stratification from 80 to 100 m is weak $N = 1.2$ cph. The Thorpe displacement $L_D = (z_n - z_m)$ results in values ranging from -8 m to 8 m, such that $L_T = 4$ m and ε_K reaches 10^{-7} W kg $^{-1}$.

To enhance confidence in the estimation we compare ε_K and K_ρ derived from the TSM with those from the FSP framework. It has been noticed (Henye et al. 1986; Gregg 1989; Polzin et al. 2014) that the FSP framework should be used with caution in the regions with strong nonlinear interaction of internal waves, as well as in regions of density flows. Here suffice to say that the nonlinear interaction of the internal waves was observed over the shelf (Novotryasov et al. 2015) far away from the profiler mooring site deployed at the depth of 425 m. The density flows often occur during the winter season from January to early March to the west of 133°E i.e., far away from the study region. The turbulent dissipation rate (ε_K^{FSP}) and diapycnal diffusivity (K_ρ^{FSP}) derived from the FSP framework were estimated as described previously (Ostrovskii et al. 2021). The FSP framework requires knowledge of the low-wavenumber shear and strain variances (Kunze et al. 2006; Polzin et al. 2014; Lique et al. 2014). To comply with this condition, the spectra of the shear and strain had to be estimated using vertical segments spanning more than or equal to 128 dbar. Because the data for the sea near-surface layer were unavailable, the layer below the mixed layer (Lim et al. 2012) was not considered in the paper by

Ostrovskii et al. (2021). To obtain ε_K^{FSP} , we applied the following relation (Henye et al. 1986; Gregg and Kunze 1991; Polzin et al. 1995; Gregg et al. 2003; Fer et al. 2010; Meyer et al. 2015):

$$\varepsilon_K^{FSP} = \varepsilon_0 \frac{N^2}{N_0^2} \frac{(\widehat{S_z^2})^2}{(\widehat{S_{zGM}^2})^2} \frac{3(R_w + 1)}{2\sqrt{2}R_w\sqrt{R_w - 1}} \frac{f \cosh^{-1}(N/f)}{f_0 \cosh^{-1}(N_0/f_0)}, \quad (9)$$

which depends on the integrated variance in the observed vertical shear ($\widehat{S_z^2}$), which is normalized by $\langle N_{ref}^2 \rangle_t$ to account for the varied stratification and the shear-to-strain ratio (R_w) as follows

$$R_w = \frac{\widehat{S_z^2}}{\xi_z^2}, \quad (10)$$

where ξ_z is the strain, which is defined as $\xi_z = (N^2 - \langle N_{ref}^2 \rangle_t) / \langle N_{ref}^2 \rangle_t$. Note that $\sqrt{\langle N_{ref}^2 \rangle_t}$ corresponds to N in Eq. 4. S_z and ξ_z were estimated over a 4-dbar scale using data binned into 2-dbar layers. To derive N , the adiabatic leveling method (Bray and Fofonoff 1981; Polzin et al. 2014) was used. The vertical gradient of potential density was estimated from unsorted profiles over 4 dbar vertically (Fer et al. 2010; Ostrovskii et al. 2021). In Eq. 9 the constants are defined according to the modified Garrett-Munk model (Garrett and Munk 1972; Cairns and Williams 1976) for the reference latitude 32.5°N: $\varepsilon_0 = 8.0 \cdot 10^{-10}$ W kg $^{-1}$, $N_0 = 3$ cph, and $f_0 = 7.8 \cdot 10^{-5}$ rad s $^{-1}$. At the observational site at 42.6° N in the northwestern Sea, the local inertial frequency was $f = 9.87 \cdot 10^{-5}$ rad s $^{-1}$. Note that relation (10) depends on the vertical shear, which was estimated from high-vertical-resolution measurements of the horizontal velocity components (see the above Sec. 2). The integrated variances $\widehat{S_z^2}$ and ξ_z^2 were calculated for overlapping 128-dbar segments with an 8-dbar spacing. It was found that throught the water column shear and strain spectra

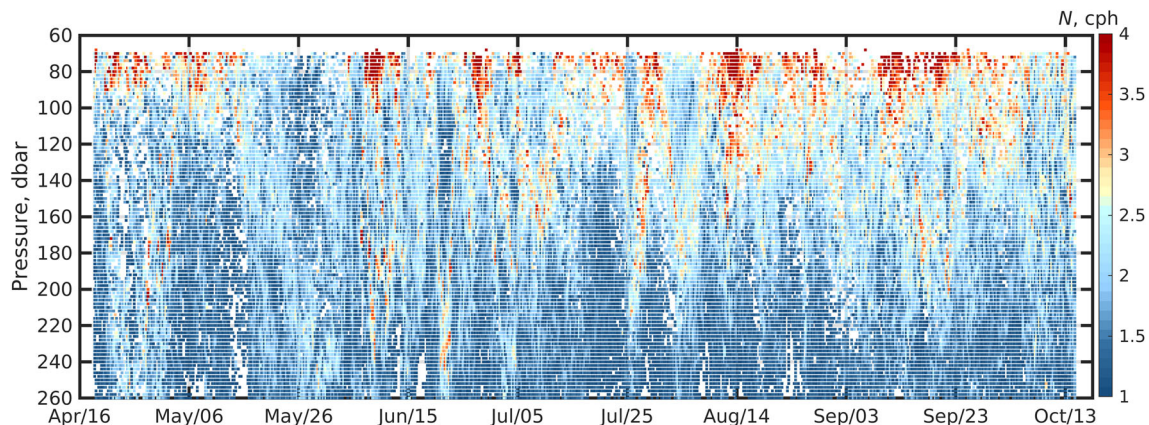


Fig. 3 The time-depth plot of the buoyancy frequency (N) estimated from all profiles. Values of $N < 10^{-1}$ cph were excluded from the analysis. The white dots indicate the regions of the data profiles that experienced favorable conditions for double diffusion

obtained using the 128-dbar segments and higher were most close to the Garrett-Munk spectra (Ostrovskii et al. 2021). Using relation Eq. 9, ε_K^{FSP} is estimated for the layers with weak density stratification, where the strain estimates are less reliable. Then, to estimate K_ρ^{FSP} , the Osborn relation Eq. 4 was applied. The ε_K^{FSP} and K_ρ^{FSP} profiles were binned into a 10-m thick layers.

4 Results

4.1 Necessary conditions for shear-driven turbulence

When analyzing the vertical mixing associated with shear-driven turbulence, the necessary conditions for its generation should be considered. Density stratification is a leading factor influencing the shear-driven turbulence evolution. A high density stratification unfavorably affects the development of shear-driven turbulence. By contrast, the extent (spatial scale) of the turbulence motion is large for weak density stratification. The values of N reach high values of more than 3 cph in the upper layer at the depth from 65 to 150 m (Fig. 3). From mid-April to the end of May, maximum N values ranging from 2.5 to 3 cph are found below the mixed layer and down to the depth of 100 m. From June to October, the maximum values of N occur at the depths ranging from 65 to 180 m. At the depths greater than 200 m, density stratification weakens, and the value of N decreases from 2.6 to 1.5 cph.

We estimate the gradient Richardson number (Ri), as a principal measure of instability, according to Miles (1961) as follows:

$$Ri = \frac{N^2}{S_z^2} < 0.25, \quad (11)$$

where N and S_z were estimated over a 4-dbar scale using data binned into 2-dbar layers.

For $Ri < 0.25$, we expect that the necessary condition for the development of shear-driven turbulence is satisfied. Figure 4 shows the evolution of Ri during the survey. Notice that the regions of the data profiles where double diffusion was developed (Stepanov et al. 2023) are excluded from this analysis. In addition, the index of potential shear instability ($IPSI$) was estimated as the percentage of water columns for which $Ri < 0.25$ (Fig. 5). From mid-April to mid-June 2015, despite strong stratification in the upper layer, $Ri < 0.25$ was often observed at the depths of 70–260 m and $IPSI$ reaches its high values for both layers. However, $IPSI$ values for the upper layer were higher than these for the lower layer (Fig. 5). From end-July to September 2015, due to increasing density stratification in the upper layer, the necessary conditions were satisfied mainly at the depths deeper than 150 m and the percentage of the water column for which $Ri < 0.25$ was minimal for both layers (Fig. 5). From September to October 2015, the necessary conditions were satisfied mainly at the depths deeper than 150 m due to near-inertial waves induced by the atmospheric storms Goni and Dujan (<https://www.nasa.gov/feature/goddard/16w-northwest-pacific-ocean>) respectively during August 28–September 8 and October 4–10.

4.2 Thorpe scale estimates of ε_K and K_ρ

In this subsection, we focus on the estimates of ε_K and K_ρ obtained using the TSM and relation (4). We aim to obtain a set of estimates that match those derived earlier by using FSP framework; therefore, the same data profiles were taken for the analysis as in Ostrovskii et al. (2021).

Figure 6 shows the TSM estimates of ε_K . Note that the values of $\varepsilon_K < 10^{-12} \text{ W kg}^{-1}$ and $K_\rho < 10^{-7} \text{ m}^2 \text{ s}^{-1}$ are not shown. Additionally, if any σ_θ profile did not have at least

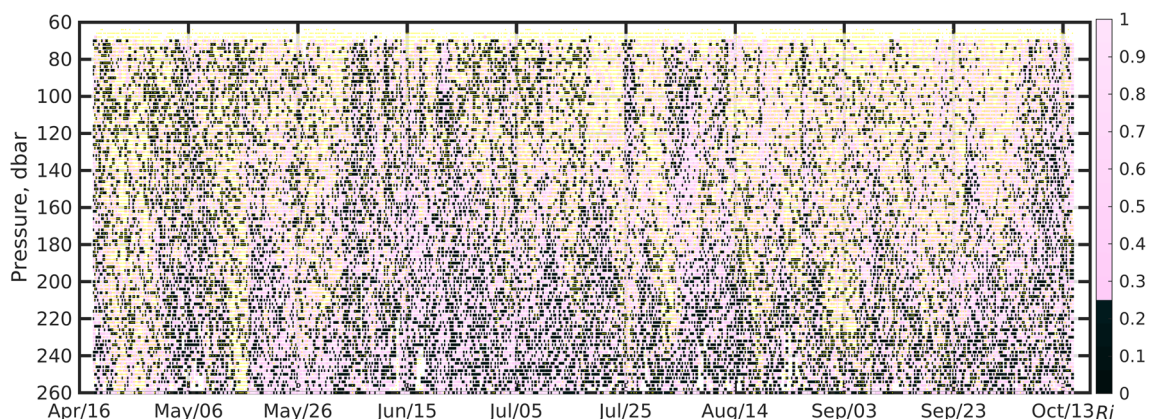
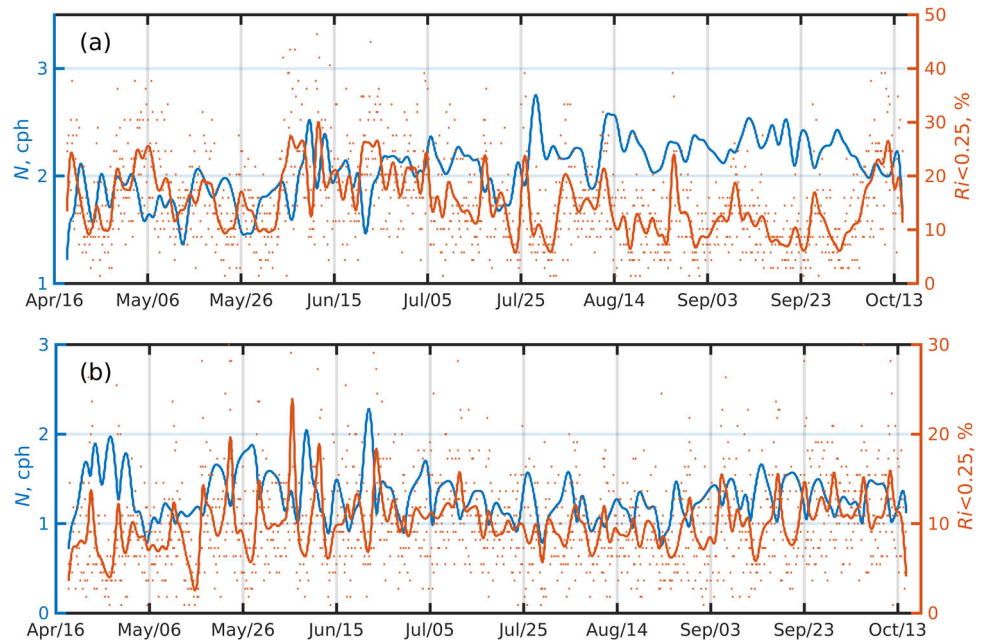


Fig. 4 The time-depth plot of the gradient Richardson number (Ri) estimated from all profiles. The yellow dots indicate the regions of the data profiles that experienced favorable conditions for double diffusion

Fig. 5 Time series of the percentage of the gradient Richardson number $Ri < 0.25$, its time-filtered series denoted by the red line and the time-filtered buoyancy frequency (N) denoted by the blue line in the upper (from 60 to 200 dbar) layer (a) and lower (from 200 to 420 dbar) layer (b)

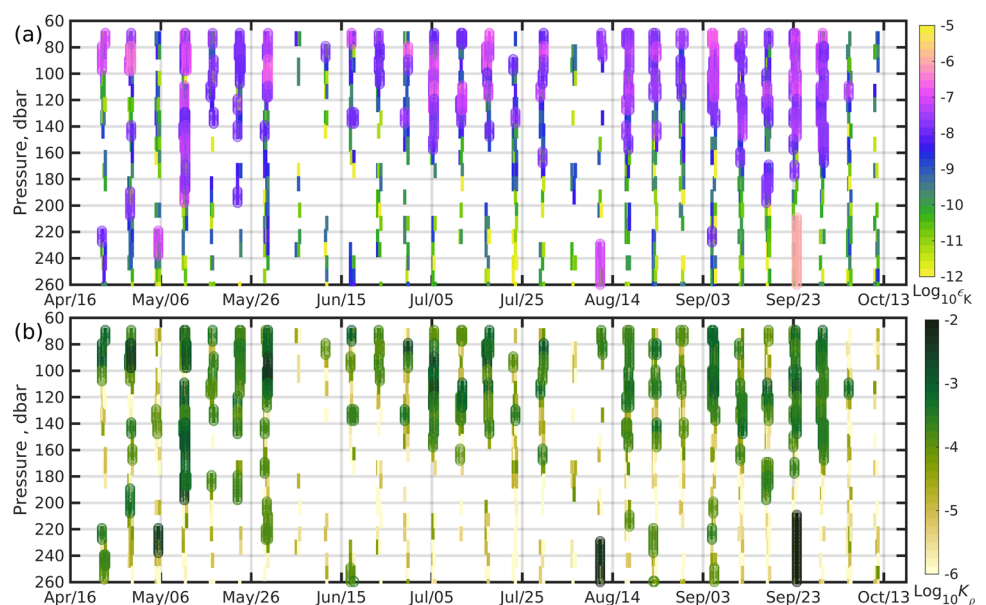


one density overturn, this profile was excluded from the analysis. In the upper layer at the depths from 70 to 150 m, the values of ϵ_K range from 10^{-9} to 10^{-7} W kg^{-1} , whereas in the lower layer at the depths from 150 to 200 m, they decrease by two orders of magnitude and become negligible at 10^{-11} W kg^{-1} . However, sometimes high values of ϵ_K occur at the depths greater than 200 m; for example, on 23 September, ϵ_K was equal to 10^{-6} W kg^{-1} . The time-depth distribution of the estimated values is rather sparse because we omit the data when other mixing processes, such as double diffusion, dominate (Stepanov et al. 2023). The high dissipation rate of turbulence results in high estimates of the diapycnal dif-

fusivity K_ρ . In particular, K_ρ is often as high as 10^{-4} – 10^{-3} $\text{m}^2 \text{s}^{-1}$ in the upper layer at the depths from 70 to 180 m (Fig. 6). Occasionally large K_ρ values in the deep layer are due to enhanced turbulent dissipation rather than weak density stratification (Fig. 3). Figure 7 shows a scatterplot of ϵ_K versus Ri . Enhanced values of $\epsilon_K > 10^{-8}$ W kg^{-1} correspond to the Richardson values being between 0.25 and 1.0.

For quantifying vertical mixing the full-depth profiles are used, which were obtained every sixth day. Due to sparseness of ϵ_K and K_ρ values in the intermediate layer from 200 to 350 dbar, their survey median values are more suitable for demonstrating typical vertical distributions of ϵ_K and K_ρ

Fig. 6 Time-depth plots of the turbulent dissipation rate (ϵ_K , W kg^{-1}) (a) and diapycnal diffusivity (K_ρ , $\text{m}^2 \text{s}^{-1}$) (b) derived using the Thorpe-scale method and full-depth data profiles. The values of $\epsilon_K > 10^{-8}$ W kg^{-1} and $K_\rho > 10^{-4}$ $\text{m}^2 \text{s}^{-1}$ are shown by large markers. The values of $\epsilon_K < 10^{-12}$ W kg^{-1} and $K_\rho < 10^{-7}$ $\text{m}^2 \text{s}^{-1}$ are not shown. Notice that the upper parts of the profiles are plotted to show the data in more detail



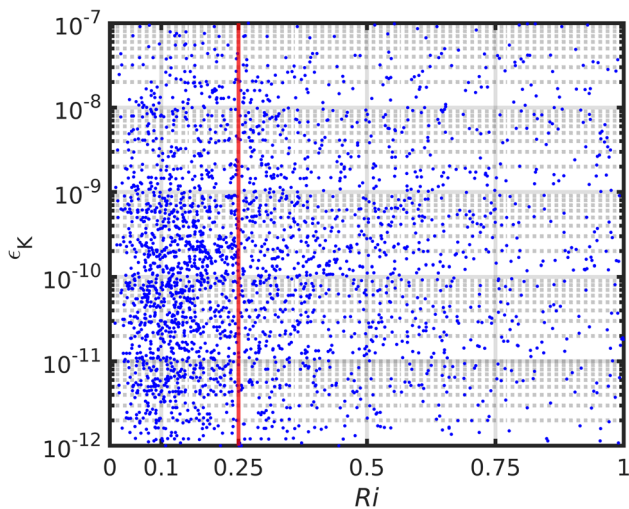
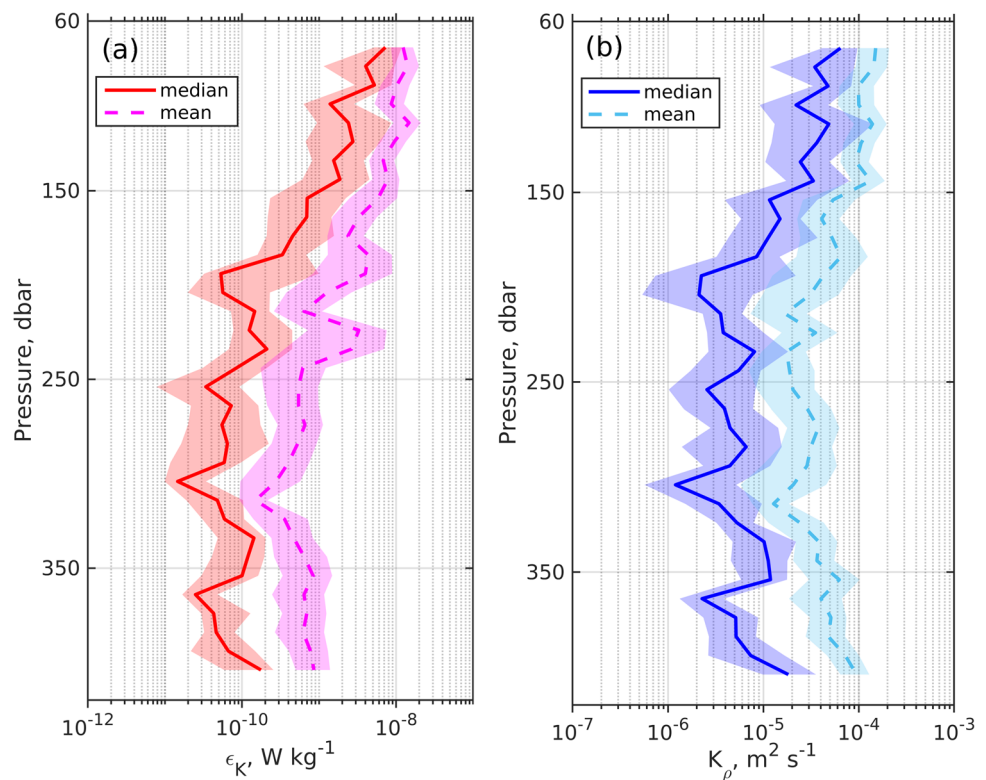


Fig. 7 The turbulent dissipation rate (ε_K , W kg^{-1}) derived using the Thorpe-scale method and full-depth data profiles versus the Richardson number (Ri). The values of $\varepsilon_K < 10^{-12} \text{ W kg}^{-1}$ are not shown

(Fig. 8). Higher survey median values from 10^{-10} to $\sim 10^{-8} \text{ W kg}^{-1}$ and from $\sim 10^{-5}$ to $10^{-4} \text{ m}^2 \text{ s}^{-1}$ are found in the upper layer at the depths from 70 to 180 m. In the depth range from 190 to 300 m, the survey median values of ε_K and K_ρ decrease to $5 \cdot 10^{-11} \text{ W kg}^{-1}$ and $5 \cdot 10^{-6} \text{ m}^2 \text{ s}^{-1}$, respectively. The uncertainty of both estimates is large, as indicated by the confidence intervals. At the depths of more than 370 m, the median survey values of ε_K and K_ρ tend to

Fig. 8 The survey-median and survey-mean profiles of the turbulent dissipation rate (ε_K) (a) and the diapycnal diffusivity (K_ρ) (b) derived by applying the Thorpe-scale method for processing the full-depth profiles of σ_θ . The 95% bootstrap confidence intervals are shown with color shading



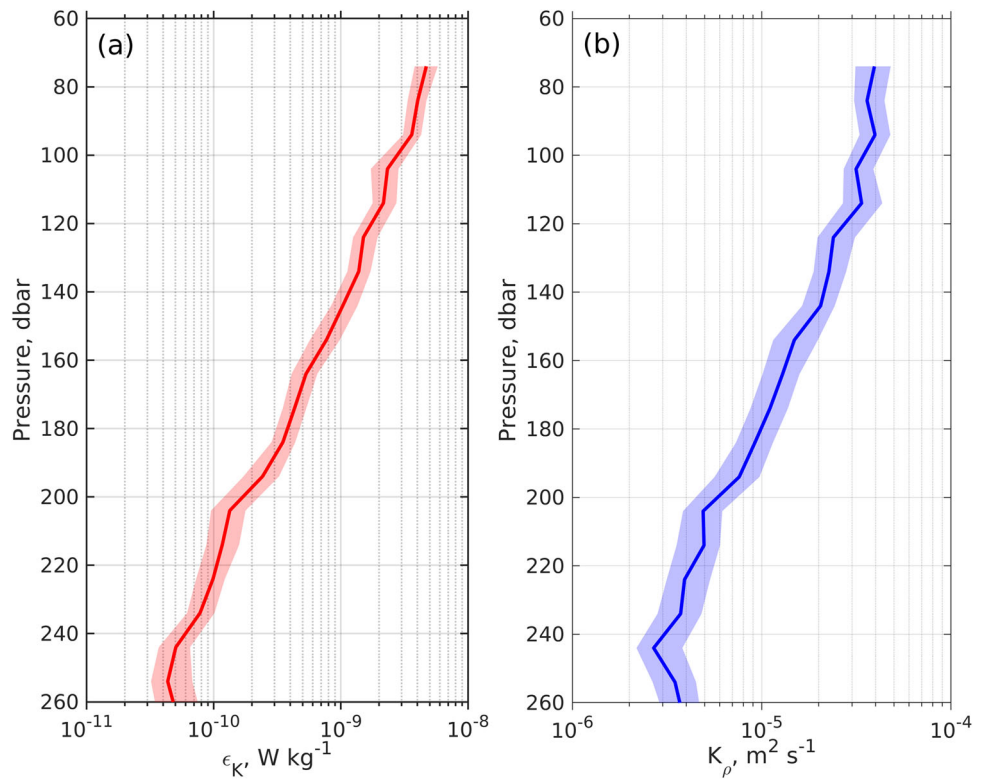
increase. The median survey values of ε_K and K_ρ increase to $\sim 10^{-10} \text{ W kg}^{-1}$ and $\sim 10^{-5} \text{ m}^2 \text{ s}^{-1}$, respectively.

Let us look at the survey-median profiles of ε_K and K_ρ for the layer at the depths 70–260 m computed from all of the data (Fig. 9), rather than only from the full-depth profiles, as shown in Fig. 8. The median survey values of ε_K peak at $3 - 4 \cdot 10^{-9} \text{ W kg}^{-1}$ in the layer at the depths from 70 to 100 m, whereas in the layer below, down to a depth of 250 m, the median survey estimates of ε_K decrease with depth to approximately $5 \cdot 10^{-11} \text{ W kg}^{-1}$. The survey-median K_ρ profile is similar to the survey-median ε_K profile. In the layer at the depths from 70 to 100 m, the survey-median K_ρ values vary from 3 to $4 \cdot 10^{-5} \text{ m}^2 \text{ s}^{-1}$, and the highest K_ρ values reach approximately $3.5 \cdot 10^{-5} \text{ m}^2 \text{ s}^{-1}$ at the depths of 100–120 m. Downward, the survey-median K_ρ decreases toward $\sim 10^{-6} \text{ m}^2 \text{ s}^{-1}$ at the depth of 250 m.

4.3 Vertical heat and salt fluxes

Estimates of diapycnal diffusivity allow us to assess the vertical fluxes of heat and salt (8). First, let us focus on the time-depth variations in Q in the upper layer (Fig. 10). The flux Q is usually directed downward during the survey. A single period was found when a Q of -6 W m^{-2} was directed upward from mid-April to May. From May through August, the median value of Q decreased from 2.2 W m^{-2} at 70 m depth to 0.1 W m^{-2} at 200 m depth. In the summer, about 20% values of Q reached a positive value of more than 10 W

Fig. 9 The survey-median values of the turbulent dissipation rate (ϵ_K) (a) and the diapycnal diffusivity (K_ρ) (b) derived by applying the Thorpe-scale method to all of the data profiles. The 95% bootstrap confidence intervals are shown with color shading



m^{-2} at the depths from 70 to 150 m. In the autumn, higher values of the flux were observed down to the depth of 180 m.

For depths greater than 200 m, the vertical heat flux decreased from June through October.

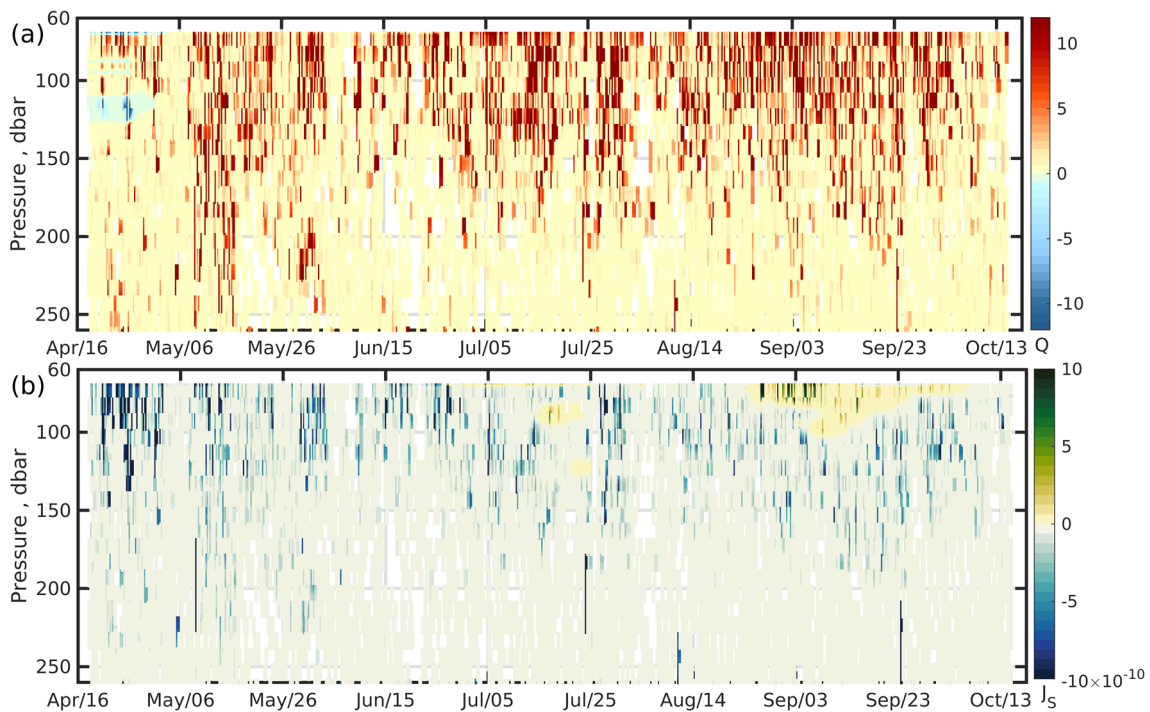


Fig. 10 Time-depth plots of the vertical heat flux (Q , W m^{-2}) (a) and salt flux (J_s , $(\text{kg salt}) (\text{kg seawater})^{-1} \text{m s}^{-1}$) (b) estimated following formula (8) from all of the data. The positive values are for the downward-directed fluxes

Figure 10 shows that J_S was mainly negative during the survey, indicating that J_S was basically directed upward. However, events associated with positive J_S values were observed in the layer at the depths from 70 to 130 m, reaching J_S of $3 \cdot 10^{-9}$ (kg salt) (kg seawater) $^{-1}$ m s $^{-1}$. High negative J_S values of $-5 \cdot 10^{-9}$ (kg salt) (kg seawater) $^{-1}$ m s $^{-1}$ were observed from mid-April through May. Additionally, the strong weakening of the J_S at the depths greater than 180 m occurred from June through October.

5 Discussion

The enhanced vertical mixing, revealed by using the TSM below the mixed layer, was associated with the basin-scale shear current. In the sea upper layer, the higher diapycnal diffusivity can be associated with the vertical shear induced by Ekman pumping. The effects of near-inertial internal waves induced by wind forcing also enhance the mixing.

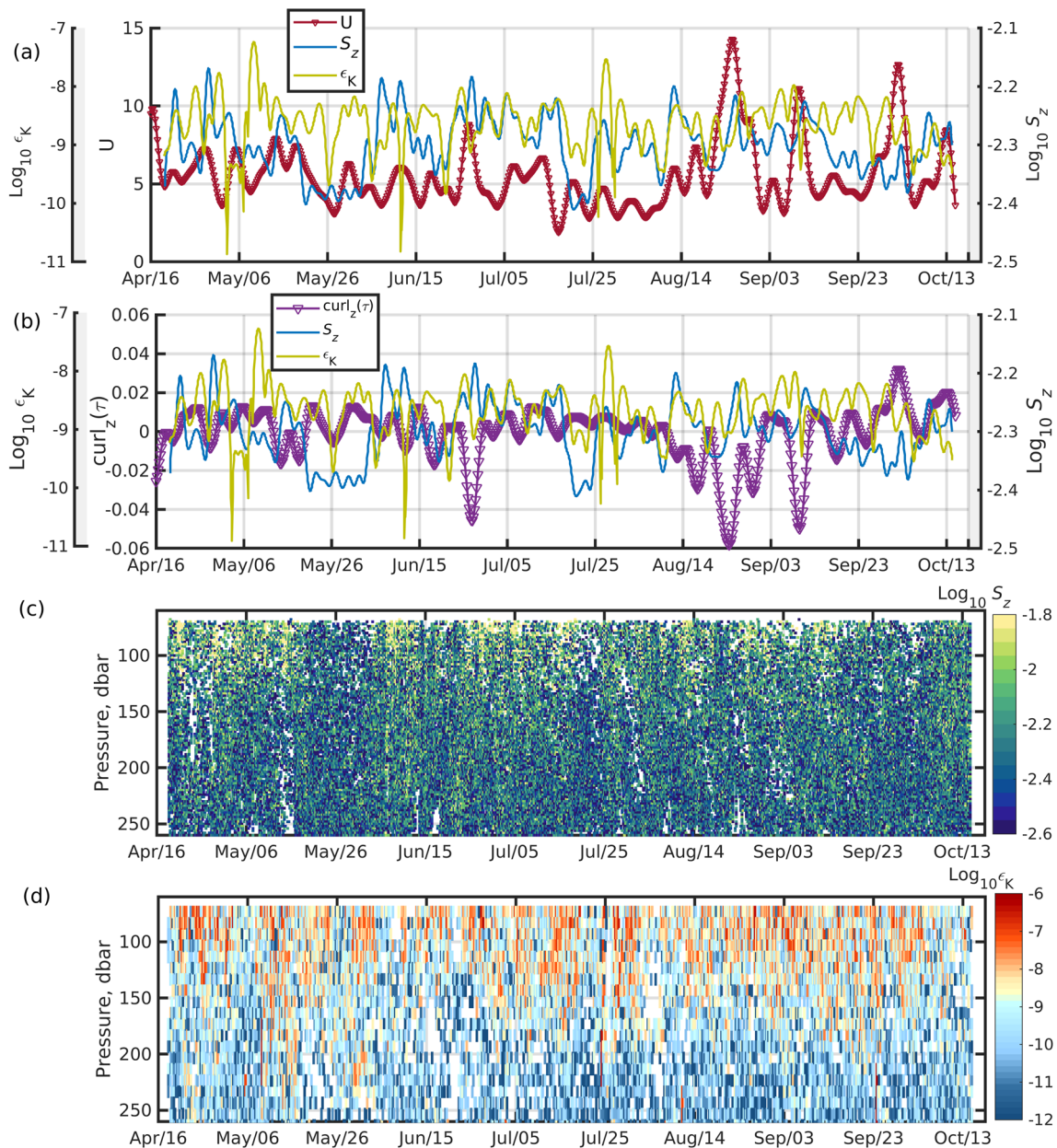


Fig. 11 Time series of the time-filtered wind speed (U , m s $^{-1}$), the depth-averaged vertical shear (S_z , s $^{-1}$) and the turbulent dissipation rate (ϵ_K , W kg $^{-1}$) in the upper layer from 64 to 200 dbar (a) and wind stress curl ($\text{curl}_z(\tau) \times 10^{-4}$, N m $^{-3}$) associated with Ekman pumping

(b) derived from the CFSv2.0 (Saha et al. 2014) atmospheric reanalysis dataset. Time-depth plots of S_z (c) and ϵ_K (d) derived using the Thorpe-scale method

Figure 11 shows wind and wind stress curl time-variations over the mooring site. The wind speed data were obtained from the atmospheric reanalysis CFSv2.0 (Saha et al. 2014) and the wind stress (τ_x, τ_y) was estimated as follows (Gill 1982)

$$(\tau_x, \tau_y) = \rho_a C_D \cdot |\mathbf{u}_{wind}| \cdot (u_{wind}, v_{wind}) \tag{12}$$

where (u_{wind}, v_{wind}) are wind speed components at the height of 10 m, ρ_a is the constant air density (1.2 kg m^{-3}) and C_D is the constant drag coefficient (0.0013). High wind speed is associated with high S_z as well as high ϵ_K from mid-April to May, mid-June to mid-July and from mid-September to October. Increasing wind stress curl from end-July to end-September resulted in increasing S_z and ϵ_K . Notice that, the sharp increasing of the wind stress curl was induced by the tropical cyclone propagation over the mooring site in September and October. The shear instabilities associated with internal waves can be important for vertical mixing in the Sea. Near-inertial oscillations are observed over the northwestern sea shelf (Yaroshchuk et al. 2016).

The Sea undergoes strong atmospheric forcing. The passage of atmospheric cycles leads to frequent adjustment of the geostrophic balance of the Sea and a release of the available potential energy. Eventually, this energy impact can result in vertical mixing in the Sea, including in the continental slope area. Notably, high turbulent dissipation rates ranging from $10^{-9} \text{ W kg}^{-1}$ to $10^{-8} \text{ W kg}^{-1}$ were observed

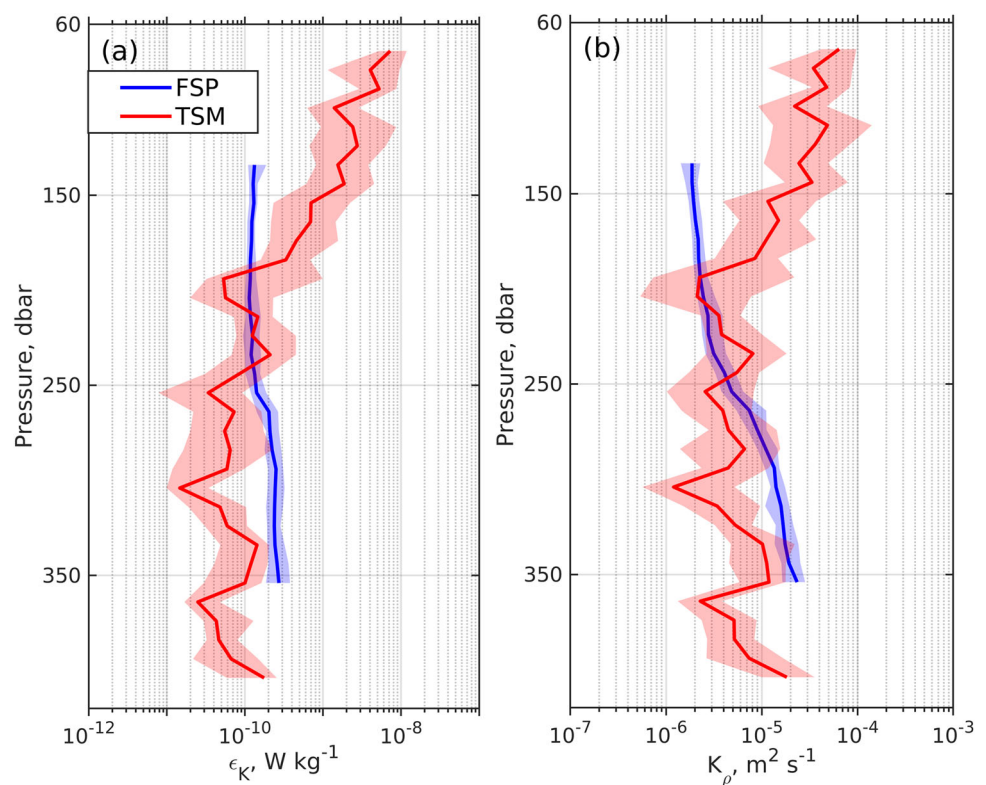
below the mixed layer in the southeastern Sea, where the Tsushima Warm Current propagates (Kawaguchi et al. 2021). Kawaguchi et al. (2021) noted that enhanced vertical mixing was modulated by mesoscale dynamics. Noticeably, the estimates obtained by Kawaguchi et al. (2021) are close to our results obtained by applying the TSM for analysis of the moored Aqualog profiler data in the Primorye Current region of the northwestern Sea. In the regions where shear flow dominates and wind forcing exhibits strong spatio-temporal variability, enhancement of vertical mixing below the mixed layer can be expected.

The intense turbulence patches under the mixed layer and the high vertical gradients of temperature and salinity often lead to the spots with enhanced vertical heat and salt exchanges. The increased vertical heat exchange was as large as 10^4 W m^{-2} with a 3-day averaged flux of about 300 W m^{-2} on the southwestern boundary of the Ulleung Basin in the Sea (Wijesekera et al. 2022), where vertical mixing was studied using combined ship-based, moored, and quasi-autonomous observations. Notice that Wijesekera et al. (2022) highlighted the enhanced vertical mixing below the mixed layer.

5.1 Comparison of the TSM and FSP approaches for quantifying turbulent mixing

In Sect. 4, we used the TSM to quantify the vertical mixing in the layer at the depths from 70 to 150 m, which was

Fig. 12 The survey-median turbulent dissipation rate (ϵ_K) (a) and the diapycnal diffusivity (K_ρ) profiles (b) derived using the Thorpe-scale method (TSM, red lines) and the finescale parameterization framework (FSP, blue lines) from the full-depth data profiles. The 95% bootstrapped confidence intervals are shown with corresponding color shading

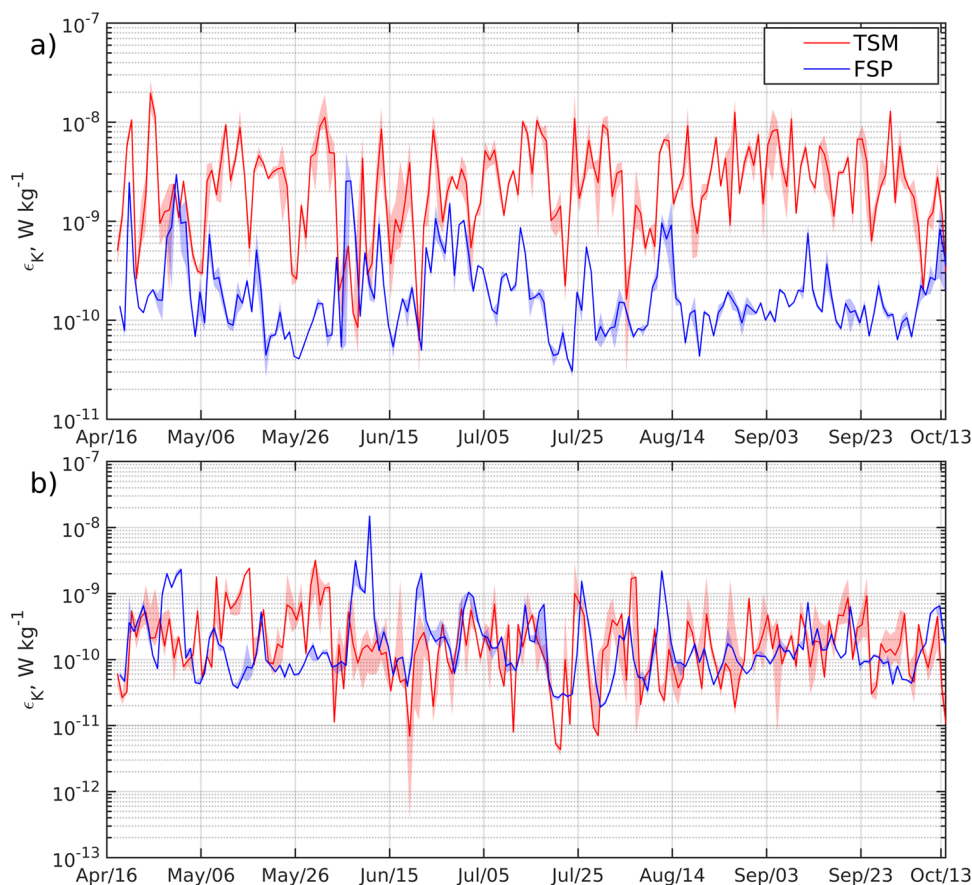


not considered in previous work, partly due to limitations of the FSP framework (Ostrovskii et al. 2021). On the one hand, the TSM has known constraints. This method should apply to shear-driven turbulence and not necessarily to either convective or double-diffusive situations. Moreover, due to weak density stratification, the turbulent dissipation rate can be underestimated. On the other hand, the FSP framework has its own limitations. The FSP is applied for the vertical wavelengths greater than 10 m that mediate energy transfers between large and small scales in the ocean (Polzin et al. 2014). In order to account for the impact of low wavenumbers into the shear and strain variance, the wider segment of 128 dbar was used. As consequence, the layers between 60 and 120 dbar was excluded from our consideration. In addition, despite the spectra of shear and strain were closed to these of the Garrett-Munk model from the $2\pi/10$ to low wavenumbers, the impact of the high wavenumbers into the spectra of shear and strain could be underestimated. The two methods can potentially complement each other if the TSM is applied to the upper portion of the sea water column and the FSP is used for the deeper layers. Furthermore, comparison of the results obtained by both methods will be useful for better understanding of their utility.

We compare the median survey values of ε_K and K_ρ estimated using the TSM (Fig. 8) and those derived by Ostrovskii et al. (2021) using the FSP framework (ε_K^{FSP} and K_ρ^{FSP}). It should be stressed that here we consider the estimates from the full-depth data profiles.

Figure 12 shows the survey-median values of the turbulent dissipation rates derived using the TSM and the FSP framework. Note that the survey median ε_K^{FSP} was derived for the depth range between 120 m and 360 m. In the layer at the depths from 120 m to 180 m, the survey-median values of ε_K are significantly greater than the survey-median values of ε_K^{FSP} . The survey-median ε_K ranged from 10^{-10} to 10^{-8} W kg^{-1} , while the survey-median values ranged between $2 \cdot 10^{-10}$ and 10^{-10} W kg^{-1} . The difference between the survey-median values of ε_K and ε_K^{FSP} decreases with increasing depth to 180 m. In the layer at the depths from 180 to 250 m, both estimates have the same order of magnitude, although the survey-median ε_K varies more widely between $5 \cdot 10^{-11}$ and $1 \cdot 10^{-10}$ W kg^{-1} . In the deeper layers from 250 to 320 m, the survey median ε_K^{FSP} is 3 to 10 times greater than the survey median ε_K , which does not exceed 10^{-10} W kg^{-1} . Note that at the depths from 320 to 350 m, the survey-averaged ε_K values increase to $1.5 \cdot 10^{-10}$ W kg^{-1} .

Fig. 13 Daily mean time series of the depth-median values of the turbulent dissipation rate derived using the Thorpe-scale method (TSM, red lines) and the finescale parameterization framework (FSP, blue lines) from all of the data binned into two layers: (a) at the depths of 70–150 m and (b) at the depths of 150–250 m



Overall, in the upper layer at the depths from 70 to 150 m, the FSP framework underestimates the turbulent dissipation due to the omission of the vertical shortwave disturbance contribution to the shear and strain variances. By contrast, TSM estimations based on high-vertical-resolution measurements can account for this contribution. When the depth increases, the contribution of the vertical shortwave disturbances to the turbulent dissipation rate decreases; thus, the estimates of the survey-median ε_K become closer to the estimates of the survey-median ε_K^{FSP} . At the depths greater than 250 m, the lower values of the survey-median ε_K may be caused by underestimation due to weak stratification.

The difference between the survey-median estimates of ε_K and ε_K^{FSP} leads to discrepancies between the survey-median values of K_ρ and K_ρ^{FSP} given the nonlinear dependence of N^2 on depth. Substantial discrepancies occur in the layer at the depths from 70 to 200 m, where the survey-median estimates of K_ρ obtained by using the TSM exceed by more than one order of magnitude the estimates derived using the FSP framework. In the deep layer at the depths from 270 m to 350 m, the survey median K_ρ^{FSP} is approximately five times greater than the survey median K_ρ .

Finally, let us compare the turbulent dissipation rates derived by applying both methods to the data binned into two layers as follows: the upper layer at the depths from 70 to 150 m and the lower layer at the depths from 150 to 250 m (Fig. 13). Notice that here we analyze the daily median values of the dissipation rates.

In the upper layer, the depth-median values of $\varepsilon_K \approx 1.2 \cdot 10^{-9} \text{ W kg}^{-1}$ usually exceed those of $\varepsilon_K^{FSP} \approx 1.2 \cdot 10^{-10} \text{ W kg}^{-1}$ by one order of magnitude (Fig. 13). By contrast, at the depths of 150 m to 250 m, the median values of ε_K and ε_K^{FSP} are often close to each other (Fig. 13). In this layer, the vertical longwave disturbances dominate the variations of vertical shear and strain. Their spectra are similar to Garrett-Munk spectra (Ostrovskii et al. 2021), and the FSP framework is better suited for estimating the turbulent dissipation rate. Notice that in the lower layer, the TSM may underestimate the turbulent dissipation rate due to weakening of the density stratification, reducing the accuracy of the estimate of the turbulent patch length. The cross-evaluation of both methods is helpful for understanding the uncertainties involved in the estimation of the turbulent dissipation rate.

5.2 Depth profile of the diapycnal diffusivity compiled from two sets of estimates based on the TSM and FSP approach

To model realistic mixing in a numerical simulation, the proper parameterization must be specified using resolved scale parameters. Based on the survey-median estimates of

K_ρ and K_ρ^{FSP} (Fig. 14), it is desirable to compile a profile of diapycnal diffusivity accounting for the features of vertical mixing addressed by both TSM and FSP. The upper part of the survey-median K_ρ profile provides a better description of the combined profile of the diapycnal diffusivity in the depth range from 70 to approximately 190 m because the TSM correctly accounts for the contribution of shortwave disturbances. In the mid-depth range from 190 to 280 m, the estimated survey-median values of K_ρ and K_ρ^{FSP} obtained by both methods are rather close to each other. Finally, in the lower part from 280 to 350 m depth, the survey-median K_ρ^{FSP} values better represented the combined profile of the diapycnal diffusivity. Overall, a strong nonlinear change in diapycnal diffusivity with depth is observed. Below the mixed layer (from 65 to 190 m) where the density stratification is strong, the combined diapycnal diffusivity exhibits two maxima. One of these is associated with the lower boundary of the mixed layer, and the other is associated with the layer with maximal values of S_z (see Ostrovskii et al. 2021). Below, a quasi-exponential decrease of the diapycnal diffusivity is observed (from $8 \cdot 10^{-5}$ to $10^{-5} \text{ m}^2 \text{ s}^{-1}$). At the depths of 180–250 m, a weakly stratified layer is present, where the combined diapycnal diffusivity varies from $3 \cdot 10^{-6} \text{ m}^2 \text{ s}^{-1}$

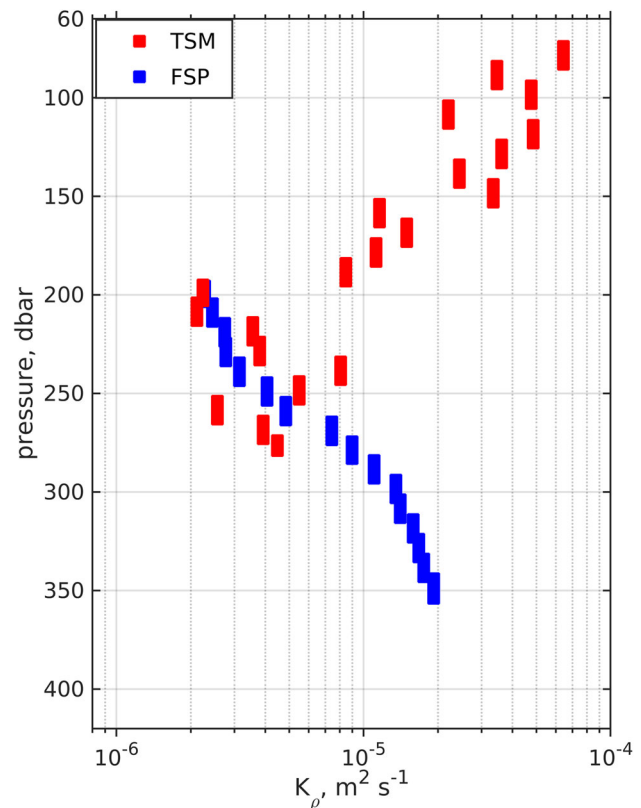


Fig. 14 The combined diapycnal diffusivity data composed of survey median values of diapycnal diffusivity K_ρ and K_ρ^{FSP} derived via the Thorpe-scale method (TSM, red bars) and the finescale parameterization framework (FSP, blue bars), respectively

to $10^{-5} \text{ m}^2 \text{ s}^{-1}$. This depth range includes the upper boundary of the East Sea Intermediate Water (ESIW) (Yoshikawa et al. 1999; Yoon and Kawamura 2002; Yamada et al. 2004; Lee et al. 2011; Park et al. 2014; Park and Lim 2018). The low values of the combined diapycnal diffusivity suggest that only short-term events associated with mesoscale eddies and strong near-inertial waves, as well as double diffusion processes, may be responsible for the intermittently higher diffusivity and vertical exchange between the ESIW and the upper layer (Ostrovskii et al. 2021; Stepanov et al. 2023). In the lower part of the water column, the increase in the combined diapycnal diffusivity with depth can be associated with the interaction of shear flow (Primorye Current) with the continental slope. Such interactions can induce enhanced mixing associated with arrested lee waves (Legg and Klymak 2008; Klymak et al. 2010). In this layer, the combined diapycnal diffusivity increases from $8 \cdot 10^{-6} \text{ m}^2 \text{ s}^{-1}$ to $2 \cdot 10^{-5} \text{ m}^2 \text{ s}^{-1}$. Notably, enhanced vertical mixing near the bottom was found in various regions of the open ocean, where the diapycnal diffusivity reached a value higher than $10^{-4} \text{ m}^2 \text{ s}^{-1}$ (Kunze et al. 2002). Diapycnal diffusivity reaches a value of $5 \cdot 10^{-5} \text{ m}^2 \text{ s}^{-1}$ near the Yermak Plateau (Fer et al. 2010) and reaches approximately $10^{-4} \text{ m}^2 \text{ s}^{-1}$ in the Storfjorden Fjord (Fer 2006).

6 Conclusions

This study addressed the vertical mixing induced by shear-driven turbulence in the continental slope region of the northwestern Sea. Based on the high-resolution vertical profiles of temperature and salinity obtained by an Aqualog profiler, the spatial scales of the turbulent patches in the density profiles were estimated using the Thorpe-scale method. Based on the relation between the Ozmidov and Thorpe scales and the Osborn relation, the turbulent dissipation rate and the diapycnal diffusivity were obtained in the intermediate layer at the depths from 70 to 260 m. The vertical heat and salt fluxes in this layer were also derived. Quantitative estimates of the turbulent mixing showed that in the depth range from 70 to 150 m, the turbulent dissipation rate and the diapycnal diffusivity reached higher values relative to the underlying water layer at the depth greater than 150 m. Strong turbulent mixing resulted in the intensification of the vertical turbulent exchange of heat and salt. The downward vertical heat flux could exceed 10.0 W m^{-2} , and the upward vertical salt flux ranged from $-5 \cdot 10^{-9}$ to $3 \cdot 10^{-9}$ (kg salt) $(\text{kg seawater})^{-1} \text{ m s}^{-1}$.

We compared the survey-median full-depth profiles of the turbulent dissipation rate derived by using the Thorpe-scale method and the finescale parameterization framework and found that both estimates were of the same order of magnitude only in the layer at the depths from 200 to 280 m. In the

upper layer at the depths from about 70 to 150 m, the Thorpe-scale method estimate of the turbulent dissipation rate was significantly (approximately one order of magnitude) greater than that of the finescale parameterization framework. We suppose that this difference is due to the limitations of the finescale parameterization framework, which does not fully account for the contribution of vertical shortwave disturbances to the shear and strain variations. By contrast, for the lower part of the water column at the depth greater than 260 m, we found that the turbulent dissipation rate estimated using the finescale parameterization framework tends to be higher than that derived using the Thorpe-scale method. This discrepancy may be associated with the limitations of the Thorpe scale method under weak density stratification. Smith (2020) modified the Thorpe-scale method by estimating the available overturn potential energy and ignoring the above-mentioned discrepancies under weak density stratification. We hope to apply Smith's approach in our future studies. In our opinion, the Thorpe-scale method yields a robust estimate of the vertical mixing intensity in the subsurface layer, and the finescale parameterization framework is more suitable for application to the deeper layer. This comparison highlights the necessity of choosing appropriate methods and frameworks to obtain reliable quantitative estimates of the vertical mixing intensity from the surface to the bottom of the sea in regions with strong seasonal variations in stratification and multiscale dynamics.

The generalized profile for diapycnal diffusivity includes the estimates of diapycnal diffusivity obtained using both the Thorpe-scale method and finescale parameterization framework. This model shows strong nonlinear behavior with depth and can be useful for improving the performance of high-resolution ocean general circulation models of basin-wide cyclonic gyre in the northern part of the Sea.

Acknowledgements This work was supported by the Russian Science Foundation, grant no. 23-27-00333, <https://rscf.ru/project/23-27-00333/>.

Data Availability Statement The datasets generated during the current study are available https://mda.vliz.be/directlink.php?fid=VLIZ_0001409_661f2d06e569c657593029.

Declarations

Conflict of Interest The authors declare no competing interests.

References

- Amante C, Eakins BW (2009) ETOPO1 1 Arc-Minute Global Relief model: Procedures, Data Sources and Analysis. Report, NOAA Technical Memorandum NESDIS NGDC-24. <https://doi.org/10.7289/V5C8276M>

- Bray NA, Fofonoff NP (1981) Available potential energy for MODE eddies. *J Phys Oceanogr* 11(1):30–47. [https://doi.org/10.1175/1520-0485\(1981\)011<0030:apefme>2.0.co;2](https://doi.org/10.1175/1520-0485(1981)011<0030:apefme>2.0.co;2)
- Cairns JL, Williams GO (1976) Internal wave observations from a mid-water float, 2. *J Geophys Res* 81(12):1943–1950. <https://doi.org/10.1029/JC081i012p01943>
- Chang KI, Zhang CI, Park C et al (2015) *Oceanography of the East Sea (Japan Sea)*. Springer. <https://doi.org/10.1007/978-3-319-22720-7>
- Dillon TM (1982) Vertical overturns: a comparison of Thorpe and Ozmidov length scales. *J Geophys Res* 87(C12). <https://doi.org/10.1029/JC087iC12p09601>
- Dougherty JP (1961) The anisotropy of turbulence at the meteor level. *J Atmos Terr Phys* 21(2–3):210–213. [https://doi.org/10.1016/0021-9169\(61\)90116-7](https://doi.org/10.1016/0021-9169(61)90116-7)
- Efron B, Gong G (1983) A leisurely look at the Bootstrap, the Jackknife, and a leisurely look at the Bootstrap, the Jackknife, and. *Am Stat* 37(1):36–48
- Fer I (2006) Scaling turbulent dissipation in an Arctic fjord. *Deep-Sea Res Pt II* 53(1–2):77–95. <https://doi.org/10.1016/j.dsr2.2006.01.003>
- Fer I, Skogseth R, Geyer F (2010) Internal waves and mixing in the Marginal Ice Zone near the Yermak Plateau. *J Phys Oceanogr* 40(7):1613–1630. <https://doi.org/10.1175/2010jpo4371.1>
- Fofonoff N, Millard Jr R (1983) Algorithms for the computation of fundamental properties of seawater. UNESCO Technical Papers in Marine Sciences; 44 p 53. <https://doi.org/10.25607/OBP-1450>
- Gamo T, Nakayama N, Takahata N et al (2014) The sea of Japan and its unique chemistry revealed by time-series observations over the last 30 years. *Monographs on Environment, Earth and Planets* 2(1):1–22. <https://doi.org/10.5047/meep.2014.00201.0001>
- Garrett C, Munk W (1972) Oceanic mixing by breaking internal waves. *Deep-Sea Res Oceanogr Abstr* 19(12):823–832. [https://doi.org/10.1016/0011-7471\(72\)90001-0](https://doi.org/10.1016/0011-7471(72)90001-0)
- Gill A (1982) *Atmosphere–Ocean Dynamics*. Academic, San Diego
- Gregg MC (1989) Scaling turbulent dissipation in the thermocline. *J Geophys Res* 94(C7):9686. <https://doi.org/10.1029/JC094iC07p09686>
- Gregg MC, Kunze E (1991) Shear and strain in Santa Monica Basin. *J Geophys Res* 96(C9). <https://doi.org/10.1029/91jc01385>
- Gregg MC, Sanford TB, Winkel DP (2003) Reduced mixing from the breaking of internal waves in equatorial waters. *Nature* 422(6931):513–515. <https://doi.org/10.1038/nature01507>
- Gregg MC, D’Asaro EA, Riley JJ et al (2018) Mixing efficiency in the ocean. *Ann Rev Mar Sci* 10:443–473. <https://doi.org/10.1146/annurev-marine-121916-063643>
- Heney FS, Wright J, Flatté SM (1986) Energy and action flow through the internal wave field: an eikonal approach. *J Geophys Res* 91(C7):8487. <https://doi.org/10.1029/JC091iC07p08487>
- Hibiya T, Furuichi N, Robertson R (2012) Assessment of fine-scale parameterizations of turbulent dissipation rates near mixing hotspots in the deep ocean. *Geophys Res Lett* 39(24). <https://doi.org/10.1029/2012gl054068>
- Inoue R, Yamazaki H, Wolk F et al (2007) An estimation of Buoyancy flux for a mixture of turbulence and double diffusion. *J Phys Oceanogr* 37(3):611–624. <https://doi.org/10.1175/jpo2996.1>
- Jeon C, Park JH, Varlamov SM et al (2014) Seasonal variation of semidiurnal internal tides in the East/Japan Sea. *J Geophys Res* 119(5):2843–2859. <https://doi.org/10.1002/2014JC009864>
- Kawaguchi Y, Wagawa T, Yabe I et al (2021) Mesoscale-dependent near-inertial internal waves and microscale turbulence in the Tsushima Warm Current. *J Oceanogr* 77(2):155–171. <https://doi.org/10.1007/s10872-020-00583-1>
- Kim K, Kim KR, Min DH et al (2001) Warming and structural changes in the east (Japan) Sea: a clue to future changes in global oceans? *Geophys Res Lett* 28(17):3293–3296. <https://doi.org/10.1029/2001GL013078>
- Kim G, Kim K, Kim K et al (2002) A sudden bottom-water formation during the severe winter 2000–2001: the case of the East/Japan Sea. *Geophys Res Lett* 29(8):71–75. <https://doi.org/10.1029/2001GL014498>
- Klymak JM, Legg S, Pinkel R (2010) A simple parameterization of turbulent tidal mixing near supercritical topography. *J Phys Oceanogr* 40(9):2059–2074. <https://doi.org/10.1175/2010JPO4396.1>
- Kunze E, Schmitt RW, Toole JM (1995) The energy balance in a warm-core ring’s near-inertial critical layer. *J Phys Oceanogr* 25(5):942–957. [https://doi.org/10.1175/1520-0485\(1995\)025<0942:TEBIAW>2.0.CO;2](https://doi.org/10.1175/1520-0485(1995)025<0942:TEBIAW>2.0.CO;2)
- Kunze E, Rosenfeld L, Carter G et al (2002) Internal waves in Monterey Submarine Canyon. *J Phys Oceanogr* 32(6):1890–1913. [https://doi.org/10.1175/1520-0485\(2002\)032<1890:Iwimsc>2.0.Co;2](https://doi.org/10.1175/1520-0485(2002)032<1890:Iwimsc>2.0.Co;2)
- Kunze E, Firing E, Hummon JM et al (2006) Global abyssal mixing inferred from lowered ADCP shear and CTD strain profiles. *J Phys Oceanogr* 36(8):1553–1576. <https://doi.org/10.1175/jpo2926.1>
- Lee C, Chang K, Lee JH et al (2014) Vertical mixing due to double diffusion in the tropical western Pacific. *Geophys Res Lett* 41(22):7964–7970. <https://doi.org/10.1002/2014GL061698>
- Lee HJ, Park JH, Wimbush M et al (2011) Tidal effects on intermediate waters: a case study in the East/Japan sea. *J Phys Oceanogr* 41(1):234–240. <https://doi.org/10.1175/2010jpo4510.1>
- Legg S, Klymak J (2008) Internal hydraulic jumps and overturning generated by tidal flow over a tall steep ridge. *J Phys Oceanogr* 38(9):1949–1964. <https://doi.org/10.1175/2008JPO3777.1>
- Lim S, C. J. Jang ISO, Park J (2012) Climatology of the mixed layer depth in the East/Japan Sea. *J Mar Syst* 96–97:1–14. <https://doi.org/10.1016/j.jmarsys.2012.01.003>
- Lique C, Guthrie JD, Steele M et al (2014) Diffusive vertical heat flux in the Canada Basin of the Arctic Ocean inferred from moored instruments. *J Geophys Res* 119(1):496–508. <https://doi.org/10.1002/2013jc009346>
- MacKinnon J, Laurent LS, Garabato ACN (2013) Diapycnal Mixing Processes in the Ocean Interior, vol 103, Elsevier BV, pp 159–183. <https://doi.org/10.1016/b978-0-12-391851-2.00007-6>
- MacKinnon JA, Zhao Z, Whalen CB et al (2017) Climate process team on internal wave-driven ocean mixing. *Bull Amer Meteor Soc* 98(11):2429–2454. <https://doi.org/10.1175/BAMS-D-16-0030.1>
- Mater BD, Venayagamoorthy SK, Laurent LS et al (2015) Biases in thorpe-scale estimates of turbulence dissipation. Part I: assessments from large-scale overturns in oceanographic data. *J Phys Oceanogr* 45(10):2497–2521. <https://doi.org/10.1175/JPO-D-14-0128.1>
- McDougall T, Barker P (2011) Getting started with TEOS-10 and the Gibbs Seawater (GSW) Oceanographic Toolbox. CSIRO Marine and Atmospheric Research
- Meyer A, Sloyan BM, Polzin KL et al (2015) Mixing variability in the Southern Ocean. *J Phys Oceanogr* 45(4):966–987. <https://doi.org/10.1175/jpo-d-14-0110.1>
- Miles JW (1961) On the stability of heterogeneous shear flows. *J Fluid Mech* 10(04):496–508. <https://doi.org/10.1017/S0022112061000305>
- Munk W, Anderson E (1948) Notes on a theory of the thermocline. *J Mar Res* 7(3):276–295
- Nikurashin M, Ferrari R, Grisouard N et al (2014) The impact of finite-amplitude bottom topography on internal wave generation in the Southern Ocean. *J Phys Oceanogr* 44(11):2938–2950. <https://doi.org/10.1175/JPO-D-13-0201.1>
- Novotryasov VV, Stepanov DV, Yaroshchuk IO (2015) Observations of internal undular bores on the Japan/East Sea shelf-coastal region. *Ocean Dyn* 66(1):19–25. <https://doi.org/10.1007/s10236-015-0905-z>

- Osborn TR (1980) Estimates of the local rate of vertical diffusion from dissipation measurements. *J Phys Oceanogr* 10(1):83–89. [https://doi.org/10.1175/1520-0485\(1980\)010<0083:eotlro>2.0.co;2](https://doi.org/10.1175/1520-0485(1980)010<0083:eotlro>2.0.co;2)
- Ostrovskii A, Stepanov D, Kaplunenko D et al (2021) Turbulent mixing and its contribution to the oxygen flux in the northwestern boundary current region of the Japan/East sea, April–October 2015. *J Mar Syst* 224:103619. <https://doi.org/10.1016/j.jmarsys.2021.103619>
- Ostrovskii A, Kubryakov A, Shoef D et al (2023) Mesoscale Anticyclonic Eddies in the Primorye Current System of the Japan Sea in Summer. *Oceanology* 63(5):609–622. <https://doi.org/10.1134/S0001437023050107>
- Ozmidov R (1965) Certain features of the energy spectrum of oceanic turbulence. *Dokl Akad Nauk SSSR* 161(4):828–831
- Park J, Lim B (2018) A new perspective on origin of the East sea intermediate water: observations of Argo floats. *Prog Oceanogr* 160:213–224. <https://doi.org/10.1016/j.pocean.2017.10.015>
- Park KA, Kang CK, Kim KR et al (2014) Role of sea ice on satellite-observed chlorophyll-a concentration variations during spring bloom in the East/Japan Sea. *Deep-Sea Res Pt I* 83:34–44. <https://doi.org/10.1016/j.dsr.2013.09.002>
- Polzin KL, Toole JM, Schmitt RW (1995) Finescale parameterizations of turbulent dissipation. *J Phys Oceanogr* 25(3):306–328. [https://doi.org/10.1175/1520-0485\(1995\)025<0306:fpotd>2.0.co;2](https://doi.org/10.1175/1520-0485(1995)025<0306:fpotd>2.0.co;2)
- Polzin KL, Garabato ACN, Huussen TN et al (2014) Finescale parameterizations of turbulent dissipation. *J Geophys Res* 119(2):1383–1419. <https://doi.org/10.1002/2013jc008979>
- Radko T, Smith DP (2012) Equilibrium transport in double-diffusive convection. *J Fluid Mech* 692:5–27. <https://doi.org/10.1017/jfm.2011.343>
- Ruddick B (1983) A practical indicator of the stability of the water column to double-diffusive activity. *Deep Sea Research Part A, Oceanographic Research Papers* 30(10):1105–1107. [https://doi.org/10.1016/0198-0149\(83\)90063-8](https://doi.org/10.1016/0198-0149(83)90063-8)
- Saha S, Moorthi S, Wu X et al (2014) The NCEP climate forecast system version 2. *J Climate* 27(6):2185–2208. <https://doi.org/10.1175/JCLI-D-12-00823.1>
- SeaBird (2010) SBE 52-MP Moored Profiler CTD and Optional DO Sensor. Sea-Bird Electronics, Inc., Bellevue, Washington USA, available at <https://www.seabird.com>
- Smith JA (2020) A comparison of two methods using thorpe sorting to estimate mixing. *J Atmos Oceanic Technol* 37:3–15. <https://doi.org/10.1175/JTECH-D-18-0234.1>
- Stansfield K, Garrett C, Dewey R (2001) Probability distribution of the Thorpe displacement within overturns in Juan de Fuca Strait. *J Phys Oceanogr* 31(12):3421–3434. [https://doi.org/10.1175/1520-0485\(2001\)031<3421:TPDOTT>2.0.CO;2](https://doi.org/10.1175/1520-0485(2001)031<3421:TPDOTT>2.0.CO;2)
- Stepanov DV, Ostrovskii AG, Lazaryuk AY (2023) Diapycnal mixing and double diffusion over the continental slope in the Northern sea of Japan in the warm half-year. *Izv Atmos Ocean Phys (Engl Transl)* 59(5):572–582. <https://doi.org/10.1134/S0001433823050109>
- Takematsu M, Nagano Z, Ostrovskii AG et al (1999) Direct measurements of deep currents in the northern Japan Sea. *J Oceanogr* 55(2):207–216. <https://doi.org/10.1023/A:1007842013257>
- Talley LD, Lobanov V, Ponomarev V et al (2003) Deep convection and brine rejection in the Japan Sea. *J Geophys Res* 30(4):1159. <https://doi.org/10.1029/2002gl016451>
- Talley LD, Min DH, Lobanov V et al (2006) Japan/East sea water masses and their relation to the Sea’s Circulation. *Oceanography* 19(3):32–49. <https://doi.org/10.5670/oceanog.2006.42>
- Thompson AF, Gille ST, MacKinnon JA et al (2007) Spatial and temporal patterns of small-scale mixing in Drake Passage. *J Phys Oceanogr* 37(3):572–592. <https://doi.org/10.1175/JPO3021.1>
- Thorpe S (1977) Turbulence and mixing in a Scottish Loch. *Philos Trans Roy Soc London* 286(1334):125–181. <https://doi.org/10.1098/rsta.1977.0112>
- Trusenkova OO, Ostrovskii AG, Lazaryuk AY et al (2021) Evolution of the thermohaline stratification in the Northwestern Sea of Japan: mesoscale variability and intra-annual fluctuations. *Oceanology* 61(3):319–328. <https://doi.org/10.1134/S0001437021030152>
- Waterhouse AF, MacKinnon JA, Nash JD et al (2014) Global patterns of diapycnal mixing from measurements of the turbulent dissipation rate. *J Phys Oceanogr* 44(7):1854–1872. <https://doi.org/10.1175/jpo-d-13-0104.1>
- Whalen CB, MacKinnon JA, Talley LD et al (2015) Estimating the mean diapycnal mixing using a finescale strain parameterization. *J Phys Oceanogr* 45(4):1174–1188. <https://doi.org/10.1175/jpo-d-14-0167.1>
- Wijesekera HW, Jarosz E, Wang DW et al (2022) Tidally driven mixing “Hot Spot” at the entrance of the Japan/East sea. *Geophys Res Lett* 49(18):1–10. <https://doi.org/10.1029/2022GL100315>
- Wunsch C, Ferrari R (2004) Vertical mixing, energy, and the general circulation of the oceans. *Annu Rev Fluid Mech* 36:281–314. <https://doi.org/10.1146/annurev.fluid.36.050802.122121>
- Yamada K, Ishizaka J, Kim SYHC et al (2004) Seasonal and interannual variability of sea surface chlorophyll a concentration in the Japan/East Sea (JES). *Prog Oceanogr* 61(2–4):193–211. <https://doi.org/10.1016/j.pocean.2004.06.001>
- Yang Q, Zhao W, Liang X et al (2017) Elevated mixing in the periphery of mesoscale eddies in the South China Sea. *J Phys Oceanogr* 47(4):895–907. <https://doi.org/10.1175/JPO-D-16-0256.1>
- Yaroshchuk I, Kosheleva A, Lazaryuk A et al (2023) Estimation of seawater hydrophysical characteristics from thermistor strings and CTD data in the sea of Japan shelf zone. *J Mar Sci Eng* 11(6). <https://doi.org/10.3390/jmse11061204>
- Yaroshchuk IO, Leont’ev AP, Kosheleva AV et al (2016) On intense internal waves in the coastal zone of the Peter the Great Bay (the Sea of Japan). *Russ Meteorol Hydro* 41(9):629–634. <https://doi.org/10.3103/s1068373916090053>
- Yoon JH, Kawamura H (2002) The formation and circulation of the intermediate water in the Japan sea. *J Oceanogr* 58(1):197–211. <https://doi.org/10.1023/A:1015893104998>
- Yoshikawa Y, Awaji T, Akitomo K (1999) Formation and circulation processes of intermediate water in the Japan Sea. *J Phys Oceanogr* 29(8):1701–1722. [https://doi.org/10.1175/1520-0485\(1999\)029<1701:Facpoi>2.0.Co;2](https://doi.org/10.1175/1520-0485(1999)029<1701:Facpoi>2.0.Co;2)
- You J, Xu Z, Li Q et al (2021) Enhanced internal tidal mixing in the Philippine Sea mesoscale environment. *Nonlinear Process Geophys* 28(2):271–284. <https://doi.org/10.5194/npg-28-271-2021>
- Zoubir A, Boashash B (1998) The bootstrap and its application in signal processing. *IEEE Signal Process Mag* 15(1):56–76. <https://doi.org/10.1109/79.647043>

Publisher’s Note Springer Nature remains neutral with regard to jurisdictional claims in published maps and institutional affiliations.

Springer Nature or its licensor (e.g. a society or other partner) holds exclusive rights to this article under a publishing agreement with the author(s) or other rightsholder(s); author self-archiving of the accepted manuscript version of this article is solely governed by the terms of such publishing agreement and applicable law.